

Probability-Based Complex-Valued Fast Iterative Shrinkage-Thresholding Algorithm for Deconvolution Beamforming

Shiyao Jiang^{ID}, Rongxin Jiang^{ID}, Xuesong Liu^{ID}, Boxuan Gu^{ID}, and Yaowu Chen^{ID}

Abstract—Conventional beamforming is widely used in sonars and radars owing to its robustness and low complexity; however, it suffers from low beam resolution and high-intensity sidelobes. Various imaging deblurring methods have been used in deconvolution beamforming to improve the beam resolution. A considerable limitation of these intensity-based methods is that the real-valued model mismatches the signals in practice and ignores the coherent information of the received signals. This study proposes a probability-based complex-valued fast iterative shrinkage-thresholding algorithm (CFISTA) to extend deconvolution beamforming to the complex domain. In this novel algorithm, the complex gradient descent and complex probability mapping are combined. Fast Fourier transform acceleration and clustering prior constraints are used on the targets to improve the efficiency and accuracy of the model. Simulation results of planar arrays show that the proposed method has superior beam resolution, sidelobe suppression, running time, and noise immunity compared with those of intensity-based methods.

Index Terms—Array signal processing, beam resolution, complex-valued fast iterative shrinkage-thresholding algorithm (CFISTA), deconvolution beamforming, sidelobe suppression.

I. INTRODUCTION

OWING to its robustness and low computational complexity, conventional beamforming (CBF) has been widely used in sonars and radars since before World War I [1], [2], [3]. Several acceleration methods have been proposed for CBF, such as sparse array and chirp zeta transform [4], [5], [6] to further reduce the computational complexity of CBF; however, these methods have slightly degraded the beam performance.

Manuscript received 7 January 2023; revised 3 June 2023, 26 October 2023, and 27 November 2023; accepted 30 November 2023. Date of publication 15 February 2024; date of current version 16 April 2024. This work was supported in part by the Fundamental Research Funds for the Central Universities and in part by the National Science Foundation for Young Scientists of China under Grant 41806115. (*Corresponding author: Rongxin Jiang*.)

Associate Editor: A. Trucco.

Shiyao Jiang is with the Institute of Advanced Digital Technology and Instrumentation, Zhejiang University, Hangzhou 310027, China (e-mail: shiyaojiang@zju.edu.cn).

Rongxin Jiang and Boxuan Gu are with Zhejiang Provincial Key Laboratory for Network Multimedia Technologies and the Institute of Advanced Digital Technology and Instrumentation, Zhejiang University, Hangzhou 310027, China (e-mail: rongxinj@zju.edu.cn; 11415011@zju.edu.cn).

Xuesong Liu and Yaowu Chen are with Embedded System Engineering Research Center, Ministry of Education of China, Hangzhou 310027, China, and also with the Institute of Advanced Digital Technology and Instrumentation, Zhejiang University, Hangzhou 310027, China (e-mail: qlhlxs@gmail.com; cyw@mail.bme.zju.edu.cn).

Digital Object Identifier 10.1109/JOE.2023.3339800

During the last decade, deconvolution methods for image inverse problems have been applied to beamforming to improve the beam resolution [7], [8], [9], [10], [11], [12], [13], [14], [15], [16], [17], [18], [19], [20], [21]. In deconvolution beamforming theory, the beam results are considered as the convolution of the targets and point spread function (PSF). The deconvolution methods aim to restore the true target distributions from the PSF and CBF results, similar to a linear inverse problem. The least-squares method is a general method used to solve this problem. In [13], a method called the deconvolution approach to the mapping of acoustic sources (DAMAS), which uses Gauss–Seidel relaxation to solve linear problems iteratively, was presented; however, it has a huge computational burden. Subsequently, Dougherty [10] proved that PSF is shift-invariant and proposed DAMAS2, which is accelerated using fast Fourier transform (FFT). A nonnegative least-squares (NNLS) algorithm with gradient projection was developed in [14] along with FFT-NNLS to replace matrix convolution with FFT. The Bayesian-based Richardson–Lucy (RL) algorithm has also been adopted to solve deconvolution beamforming [15], [16]. The CLEAN method and its variants applied to coherent scenarios have also been proposed in [17], [18], [19], and [20], which iteratively search for the current peak and reconstruct the beam pattern. These methods have shown promising results in radar image deconvolution.

A fast iterative shrinkage-thresholding algorithm (FISTA) based on accelerated gradient descent was presented in [22] and verified to have a quadratic convergence rate. Lylloff et al. [7] applied FISTA for deconvolution beamforming and showed that FISTA has a greater worst case convergence rate than ordinary gradient methods, such as FFT-NNLS.

The abovementioned methods are based on beam intensity and assume that the targets are incoherent. However, ensuring strict adherence to the assumptions of the real-valued methods in practical scenarios is challenging [23]. Moreover, the real-valued methods neglect the crucial phase information embedded within the complex signals. As the signal model is not sufficiently accurate, intensity-based methods have problems, such as increased main lobe width and weak sidelobe suppression ability in processing narrowband signals.

In this study, a probability-based complex-valued FISTA (CFISTA) is proposed for planar array imaging sonar deconvolution beamforming to retain the phase term of the beam to improve

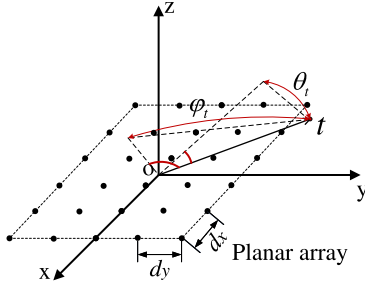


Fig. 1. Geometric model of a planar array and signal angles.

the beam performance, which can considerably improve the beam resolution and noise immunity.

The contributions of the study are summarized as follows.

- 1) We expand the gradient descent of FISTA to the complex domain using the Wirtinger derivatives and accelerate it using FFT.
- 2) A complex probability mapping module, based on the minimum mean-squared error (MMSE), replaces the original nonnegative mapping that is unavailable in the complex domain.
- 3) A cluster prior of targets was added to the probability model to fit the characteristics of beam density at the targets of sonar images, and the point estimation formula of hyperparameters was derived.
- 4) Simulations on the planar array prove that CFISTA has advantages in the main lobe width, sidelobe suppression ratio, noise immunity, running time, and image quality.

The rest of this article is organized as follows. The CBF model and intensity-based FISTA are reviewed in Section II. Section III presents the CFISTA for complex-valued deconvolution beamforming. In Section IV, CFISTA and conventional methods are examined using simulation data. Finally, Section V concludes this article.

II. DECONVOLUTION BEAMFORMING AND FISTA

A. Deconvolution Beamforming

We consider a planar receiving array containing M elements (R rows and C columns), and the horizontal and vertical spacing between each element are d_x and d_y , respectively. There is an omnidirectional transmitter located at the coordinate origin. We assume T narrowband received signals with wavelength λ from the far-field of the array, arrive as plane waves. As illustrated in Fig. 1, the direction angle of t_{th} signal is (θ_t, φ_t) , where θ_t refers to the angle between vector t and plane YOZ , and φ_t refers to the angle between vector t and plane XOZ .

Ignoring the noise term, the response of the t_{th} signal at the m element located in row r and column c is expressed as follows:

$$\begin{aligned} s_{mt} &= x_t \cdot \psi_{mt} \\ \psi_{mt} &= e^{-j \frac{2\pi}{\lambda} (cd_x \sin \theta_t + rd_y \sin \varphi_t)} \end{aligned} \quad (1)$$

where x_t indicates the receiving signal intensity, ψ_{mt} indicates the phase term, and $j = \sqrt{-1}$. The matrix form of this equation is

$$\mathbf{s} = \Psi \mathbf{x} \quad (2)$$

where $\mathbf{s} \in \mathbb{C}^M$ represents the vector of T complex received signals, $\mathbf{x} \in \mathbb{C}^T$ represents the vector of the signal complex-valued intensity, and $\Psi \in \mathbb{C}^{M \times T}$ represents the look-direction matrix of the array. The t_{th} column of Ψ corresponds to $[\psi_{t1}, \psi_{t2}, \dots, \psi_{tm}, \dots, \psi_{tM}]^T$. Generally, CBF methods divide the array observation domain into N directions, and the steering vector \mathbf{p}_n in the direction (θ_n, φ_n) is defined as follows:

$$\begin{aligned} \mathbf{p}_n &= [p_{n1}, p_{n2}, \dots, p_{nm}, \dots, p_{nM}]^T \\ p_{nm} &= \frac{1}{M} e^{-j \frac{2\pi}{\lambda} (cd_x \sin \theta_n + rd_y \sin \varphi_n)}. \end{aligned} \quad (3)$$

Referring to the model proposed in [24], for imaging sonars with nondirectional transmitters, the transmit waveform is a parameter related to the transmit frequency and independent of the steering angle. Therefore, it has little contribution to the angle-domain deconvolution. The CBF result in the direction (θ_n, φ_n) corresponds to the superposition of the array responses of the T received signals and can be expressed as follows:

$$\begin{aligned} B(\theta_n, \varphi_n) &= \mathbf{p}_n^H \mathbf{s} \\ &= \sum_{t=1}^T \frac{x_t}{M} \sum_{m=1}^M e^{j \frac{2\pi}{\lambda} [cd_x (\sin \theta_n - \sin \theta_t) + rd_y (\sin \varphi_n - \sin \varphi_t)]} \\ &= \sum_{t=1}^T x_t e^{j \frac{2\pi}{\lambda} (Cd_x u_{nt} + Rd_y v_{nt})} \frac{\text{sinc}(\pi Cd_x \frac{u_{nt}}{\lambda})}{\text{sinc}(\pi d_x \frac{u_{nt}}{\lambda})} \frac{\text{sinc}(\pi Rd_y \frac{v_{nt}}{\lambda})}{\text{sinc}(\pi d_y \frac{v_{nt}}{\lambda})} \\ &= \sum_{t=1}^T x_t \cdot \text{PSF}(\theta_t, \varphi_t, \theta_n, \varphi_n) \end{aligned} \quad (4)$$

where $\text{sinc}(x) = \sin(x)/x$, $u_{nt} = \sin(\theta_n) - \sin(\theta_t)$, and $v_{nt} = \sin(\varphi_n) - \sin(\varphi_t)$. As shown in (4), $B(\theta_n, \varphi_n)$ is also a function of $(\sin \theta_n, \sin \varphi_n)$, that is

$$B(\sin \theta_n, \sin \varphi_n) = \sum_{t=1}^T x_t \cdot \text{PSF}(\sin \theta_t, \sin \varphi_t, \theta_n, \varphi_n)$$

In intensity-based deconvolution methods, the cross term is omitted to simply the calculation or in consideration that the targets are incoherent. Thus, the beam intensity is approximately calculated as follows:

$$\begin{aligned} B_p(\sin \theta_n, \sin \varphi_n) &= |B(\sin \theta_n, \sin \varphi_n)|^2 \\ &\approx \sum_{t=1}^T |x_t|^2 \left| \frac{\text{sinc}(\pi Cd_x u_{nt}/\lambda)}{\text{sinc}(\pi d_x u_{nt}/\lambda)} \cdot \frac{\text{sinc}(\pi Rd_y v_{nt}/\lambda)}{\text{sinc}(\pi d_y v_{nt}/\lambda)} \right|^2. \end{aligned} \quad (5)$$

Under the assumption that the targets are incoherent, the array beamforming results in N directions can be regarded as a convolution of the target distribution and PSF, which is defined as follows:

$$\mathbf{B}_p = \Phi_p \mathbf{x}_p + \xi_p \quad (6)$$

where $\mathbf{B}_p \in \mathbb{R}^N$ indicates the beam intensity, $\Phi_p \in \mathbb{R}^{N \times N}$ is the real-value PSF, and $\xi_p \in \mathbb{R}^N$ is the real-value noise. When PSF does not depend on the specific position of the targets and the array, it can be considered shift-invariant [7], [25]. The PSF in (5) is expressed in terms of the sine of the direction angle and

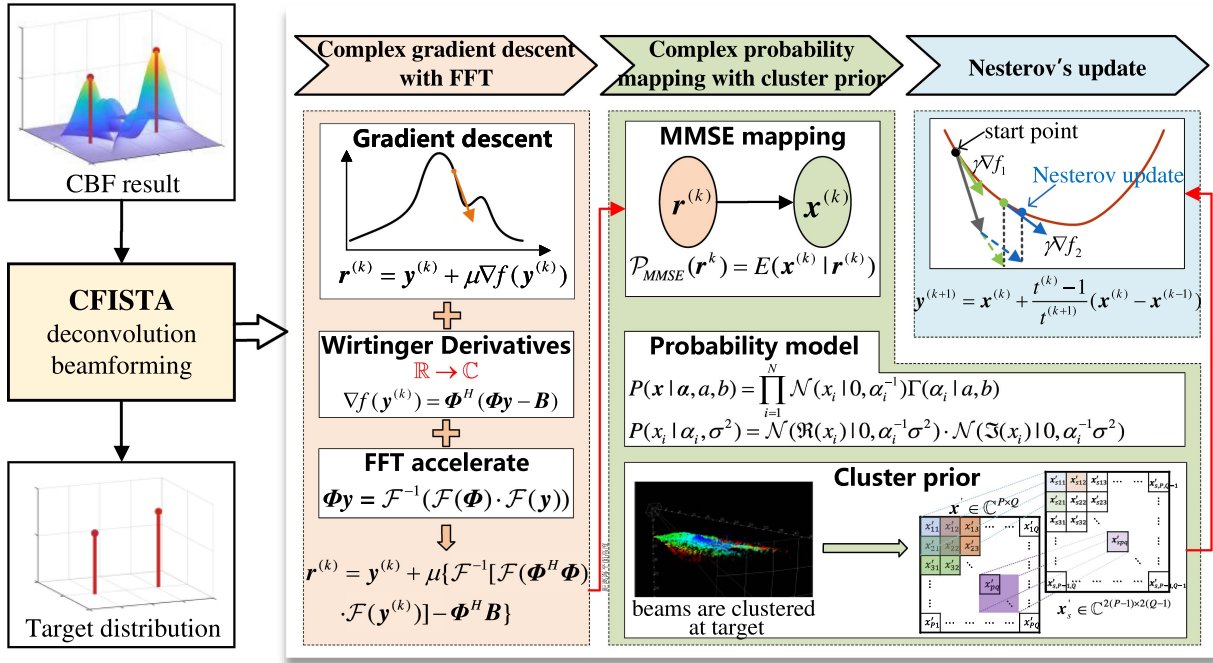


Fig. 2. Proposed probability-based CFISTA for deconvolution beamforming, which obtains accurate targets distribution by deconvolution of CBF results. CFISTA includes three parts: 1) complex gradient descent with FFT, 2) complex probability mapping with cluster prior, and 3) Nesterov's update.

is the same regardless of the target positions. Therefore, the PSF is shift-invariant.

B. Fast Iterative Shrinkage-Thresholding Algorithm

FISTA is an extension of the conventional gradient iterative algorithm, which is used in image and signal processing, and has recently been applied to acoustic beam deconvolution. FISTA accelerates convergence using the momentum update of the intermediate variables [26]. The common iterative formula of deconvolution beamforming is [7]

$$\begin{aligned} \mathbf{x}_p^{(k)} &= \mathcal{P}_+ \left(\mathbf{y}_p^{(k)} + \mu \nabla f \left(\mathbf{y}_p^{(k)} \right) \right) \\ &= \mathcal{P}_+ \left[\mathbf{y}_p^{(k)} + \mu \Phi_p^T \left(\Phi_p \mathbf{y}_p^{(k)} - \mathbf{B}_p \right) \right] \end{aligned} \quad (7a)$$

$$t^{(k+1)} = \frac{1}{2} \left(1 + \sqrt{1 + 4t^{(k)}} \right) \quad (7b)$$

$$\mathbf{y}_p^{(k+1)} = \mathbf{x}_p^{(k)} + \frac{t^{(k)} - 1}{t^{(k+1)}} \left(\mathbf{x}_p^{(k)} - \mathbf{x}_p^{(k-1)} \right) \quad (7c)$$

where superscript $.^{(k)}$ denotes the k th iteration, $\mathbf{y}_p^{(k)}$ is the intermediate variable of FISTA, ∇f indicates the gradient operator, $\mu = -1/L$ is the fixed step size, L is the Lipschitz constant of ∇f , and $t^{(k)}$ indicates the scale of the momentum update. In most methods, L is approximated as the largest eigenvalue of Hessian $\nabla^2 f = \Phi^T \Phi$. $\mathcal{P}_+(\cdot)$ is the nonnegative mapping of the gradient descent result, which truncates the minimum value of the beam after the gradient descent to zero.

The initial value of the iteration was set as $\mathbf{x}_P^{(0)} = \mathbf{y}_p^{(1)} = \mathbf{B}_p$, $t^{(0)} = 1$. The iteration then proceeds by following (7). When

$|\mathbf{x}_p^{(k)} - \mathbf{x}_p^{(k-1)}| \leq \epsilon$, the iteration ends, and $\mathbf{x}_p^{(k)}$ indicates the result of FISTA. ϵ indicates the convergence threshold.

For intensity beam deconvolution, the nonnegative mapping $\mathcal{P}_+(\cdot)$ ensures that the beam intensity conforms to constraints and has low computational complexity. However, it cannot further accelerate convergence and is not applicable to complex deconvolution.

III. COMPLEX PROBABILITY-MAPPING FISTA

As previously mentioned, intensity-based deconvolution methods assume that the received signals are incoherent. Complex-valued signals contain phase information, which is crucial for improving the accuracy of the model, meaning that the cross term in \mathbf{B} cannot be ignored. Furthermore, the rank of Φ is lacking and regular mapping is invalid in the complex domain, which affects the beam accuracy and sidelobe suppression of the deconvolution results. Considering the characteristics of coherent deconvolution beamforming, we propose complex probability-mapping FISTA to directly deconvolve complex-valued beams. The illustration of the proposed CFISTA is shown in Fig. 2.

A. Complex Gradient and Step Size

First, we focus on step size μ and gradient ∇f . Equation (4) can be rewritten as follows:

$$\mathbf{B} = \Phi \mathbf{x} + \xi \quad (8)$$

where $\mathbf{B} \in \mathbb{C}^N$ represents the beam vector with N desired directions, $\Phi \in \mathbb{C}^{N \times N}$ represents the PSF matrix, $\mathbf{x} \in \mathbb{C}^N$ represents

the target vector, and $\xi \in \mathbb{C}^N$ represents the noise vector. Φ_i indicates the i th column of Φ , which denotes the PSF in the i th direction, and is expressed as follows:

$$\begin{aligned}\Phi_i &= e^{j\frac{2\pi}{\lambda}[Cd_x u_i + Rd_y v_i]} \frac{\text{sinc}(\pi Cd_x u_i / \lambda)}{\text{sinc}(\pi d_x u_i / \lambda)} \frac{\text{sinc}(\pi R d_y v_i / \lambda)}{\text{sinc}(\pi d_y v_i / \lambda)} \\ \mathbf{u}_i &= [u_{i1}, \dots, u_{in}, \dots, u_{iN}]^T; \quad \mathbf{v}_i = [v_{i1}, \dots, v_{in}, \dots, v_{iN}]^T\end{aligned}\quad (9)$$

where $u_{in} = \sin \alpha_i - \sin \alpha_n$ and $v_{in} = \sin \beta_i - \sin \beta_n$.

The element in Φ of a uniform square array (i.e., $d_x = d_y = d$ and $R = C = M'$) is given as follows:

$$\begin{aligned}\Phi_{pq} &= e^{j\frac{2\pi}{\lambda}[M'd(u_{pq}+v_{pq})]} \frac{\text{sinc}(\pi M' d u_{pq} / \lambda)}{\text{sinc}(\pi d u_{pq} / \lambda)} \frac{\text{sinc}(\pi M' d v_{pq} / \lambda)}{\text{sinc}(\pi d v_{pq} / \lambda)} \\ &= A e^{j\frac{2\pi}{\lambda} \varphi_{pq}} \\ p &= 1, \dots, N; \quad q = 1, \dots, N\end{aligned}\quad (10)$$

where A indicates the magnitude of Φ_{pq} , φ_{pq} indicates the phase angle, and the definitions of u_{pq} and v_{pq} are the same as those in (4). Accordingly, $u_{pq} = -u_{qp}$ and $v_{pq} = -v_{qp}$. Φ_{qp} is derived as follows:

$$\Phi_{qp} = A e^{j\frac{2\pi}{\lambda}[M'd(u_{qp}+v_{qp})]} = A e^{j\frac{2\pi-\varphi_{pq}}{\lambda}} = \Phi_{pq}^*. \quad (11)$$

Thus, the complex-valued PSF matrix Φ is a Hermitian matrix; the eigenvalues of the Hessian $\nabla^2 f$ are real values, and the Lipschitz constant L is given as follows:

$$L = \max[\text{diag}(\Phi^H \Phi)]. \quad (12)$$

According to Wirtinger derivatives, the gradient of $f(\mathbf{y}^{(k)}) = \frac{1}{2} \|g(\Phi \mathbf{y}^{(k)}) - \mathbf{B}\|_2^2$ is derived as follows:

$$\begin{aligned}\nabla f &= \frac{\partial f}{\partial \mathbf{y}^*} = \left[\frac{\partial f}{\partial y_1^*}, \frac{\partial f}{\partial y_2^*}, \dots, \frac{\partial f}{\partial y_n^*} \right]^T \\ &= \Phi^H \left\{ [g(z) - \mathbf{B}]^* \frac{\partial g}{\partial z^*} + [g(z) - \mathbf{B}] \frac{\partial g^*}{\partial z^*} \right\} \\ &= \Phi^H (\Phi \mathbf{y} - \mathbf{B})\end{aligned}\quad (13)$$

where $g(z) = \Phi \mathbf{y}$. To follow the gradient calculation convention in FISTA and for brevity, (13) does not include the constant coefficient and iteration number superscript.

To determine the gradient and step size of CFISTA, (7a) is partly rewritten as follows:

$$\begin{aligned}\mathbf{r}^{(k)} &= \mathbf{y}^{(k)} + \mu \nabla f(\mathbf{y}^{(k)}) \\ &= \mathbf{y}^{(k)} + \mu \Phi^H (\Phi \mathbf{y}^{(k)} - \mathbf{B})\end{aligned}\quad (14)$$

where $\mathbf{r}^{(k)}$ denotes the gradient descent result. Since Φ is a Hermitian matrix and a function of $(\sin \theta_n, \sin \varphi_n)$, Φ is shift-invariant and can be accelerated using FFT for matrix multiplication. Equation (14) is derived as follows:

$$\mathbf{r}^{(k)} = \mathbf{y}^{(k)} + \mu \{ \mathcal{F}^{-1} [\mathcal{F}(\Phi^H \Phi) \cdot \mathcal{F}(\mathbf{y}^{(k)})] - \Phi^H \mathbf{B} \} \quad (15)$$

where \cdot denotes the Hadamard product, \mathcal{F} indicates FFT, and \mathcal{F}^{-1} indicates IFFT (inverse fast Fourier transfer). $\Phi^H \Phi$ and

$\Phi^H \mathbf{B}$ can be calculated using FFT before iterations. Accelerated by FFT, the computational complexity of the gradient descent is reduced from $O(N^2)$ to $O(N \log N)$.

B. Probability Mapping

The MMSE shrinkage unit based on the probability model is adopted in ISTA and FISTA to precisely estimate the original signal from a tentative estimate [27]. In addition, the MMSE estimator has high estimation accuracy and accelerates the convergence rate [28], which is given as follows:

$$\mathbf{x}^{(k)} = \mathcal{P}_{\text{MMSE}}(\mathbf{r}^k) \quad (16)$$

where $\mathcal{P}_{\text{MMSE}}$ is the mapping based on MMSE.

However, to the best of the authors' knowledge, there is no complex MMSE mapping for FISTA. The ISTA with a complex MMSE is mentioned in [29]; however, the specific algorithm and experimental verification are not given. Thus, we propose an MMSE mapping based on complex probability and cluster prior for narrowband signals.

Let $P(\cdot)$ be a probability density function (PDF). The MMSE estimator for the k th iteration is defined as

$$\mathcal{P}_{\text{MMSE}}(\mathbf{r}) = \mathbb{E}(\mathbf{x}|\mathbf{r}) = \sum_{i=1}^N x_i P(x_i|r_i) \quad (17)$$

where $\mathbb{E}(\mathbf{x})|\mathbf{r}$ indicates the conditional expectation and $P(x_i|r_i)$ indicates the posterior probability in the i th direction. According to the Bayesian theorem, the posterior probability is expressed as follows:

$$P(\mathbf{x}|\mathbf{r}) = \frac{P(\mathbf{x})P(\mathbf{r}|\mathbf{x})}{P(\mathbf{r})}. \quad (18)$$

Assume that $\mathbf{r} = \mathbf{Ex} + \boldsymbol{\varepsilon}$, where $\boldsymbol{\varepsilon}$ denotes a Gaussian distribution with zero mean and variance σ^2 and \mathbf{E} is the identity matrix. The conditional PDF is then obtained by

$$P(\mathbf{r}|\mathbf{x}, \sigma^2) = (2\pi\sigma^2)^{-\frac{1}{2}} e^{-\frac{\|\mathbf{r}-\mathbf{x}\|^2}{2\sigma^2}}. \quad (19)$$

In the Bayesian theory, $P(\mathbf{r})$ is observed from the data and is considered a constant; thus, the posterior can be solved as long as $P(\mathbf{x})$ is known. If the targets are sparse, the nonzero element number of \mathbf{x} is less than the desired direction N , and the prior of \mathbf{x} can be regarded a zero-mean Gaussian distribution with variance α^{-1} . A gamma prior was set on α to promote the sparsity of \mathbf{x} . The PDF of \mathbf{x} is derived as follows:

$$P(\mathbf{x}|\alpha, a, b) = \prod_{i=1}^N \mathcal{N}(x_i|0, \alpha_i^{-1}) \Gamma(\alpha_i|a, b) \quad (20)$$

where a and b are hyperparameters of α . In this study, we set $a = 1000, b = 1$. The hyperparameters are not optimized based on the simulations and experiments, which is more consistent with the fact that the prior residual $\mathbf{r} - \mathbf{x}$ is usually inaccurate. For the complex probability problem, the real and imaginary parts of \mathbf{x} are two statistically related tasks that share the same prior. The likelihood of each element in \mathbf{x} is the product of the

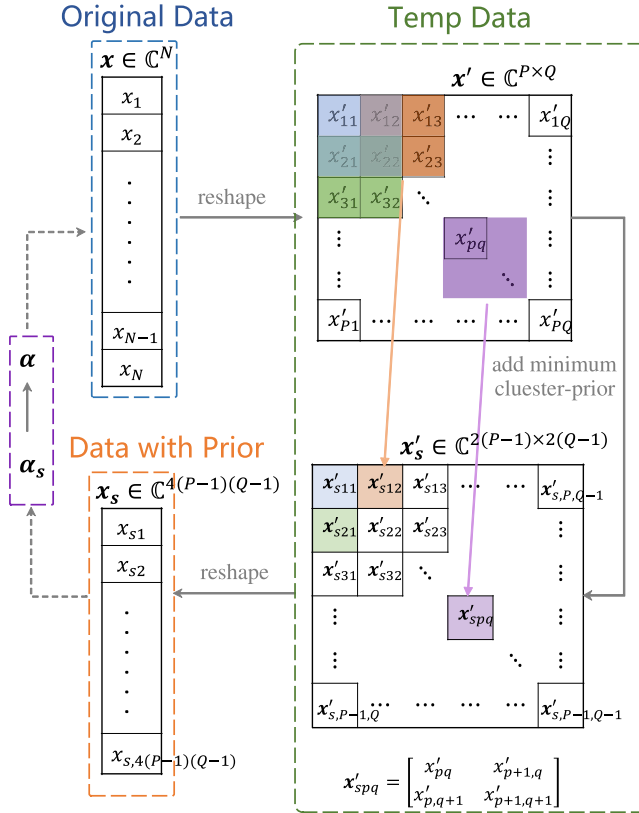


Fig. 3. Addition of a minimum scale cluster before \mathbf{x} .

real and imaginary parts, which is given as follows:

$$P(x_i|\alpha_i, \sigma^2) = \mathcal{N}(\Re(x_i)|0, \alpha_i^{-1}\sigma^2) \cdot \mathcal{N}(\Im(x_i)|0, \alpha_i^{-1}\sigma^2) \quad (21)$$

where $\Re(x_i)$ and $\Im(x_i)$ indicate the real and imaginary parts, respectively, which share the hyperparameters.

In practical applications, sonar signals are sparse in the entire observation field but dense near targets. A cluster prior was used to optimize the probability model. We applied the same control parameters to adjacent desired directions to avoid the effect of choosing the wrong basis vector on the overall estimate. We divide N desired beams into P vertical and Q horizontal beams. The process of adding the cluster prior is illustrated in Fig. 3.

We reshaped \mathbf{x} into $\mathbf{x}' \in \mathbb{C}^{P \times Q}$. Subsequently, an overlapping structure was added in the horizontal and vertical beam directions. As shown in Fig. 3, each element of the extended matrix $\mathbf{x}'_s \in \mathbb{C}^{2(P-1) \times 2(Q-1)}$ corresponds to four adjacent elements in \mathbf{x}' , whose elements are given by

$$x'_{spq} = \begin{bmatrix} x'_{pq} & x'_{p,q+1} \\ x'_{p+1,q} & x'_{p+1,q+1} \end{bmatrix}. \quad (22)$$

Following that, \mathbf{x}'_s is reshaped into vector $\mathbf{x}_s \in \mathbb{C}^{4(P-1)(Q-1)}$ to facilitate matrix calculation. Accordingly, the hyperparameter that corresponds to \mathbf{x}_s is $\boldsymbol{\alpha}_s \in \mathbb{C}^{(P-1)(Q-1)}$. Each element in $\boldsymbol{\alpha}_s$ controls the four adjacent beam-direction elements in \mathbf{x}_s . Upon solving $\boldsymbol{\alpha}_s$, $\boldsymbol{\alpha}$ is obtained from the mapping of the cluster prior, and \mathbf{x} is then calculated using (20) and (21).

For the matrix \mathbf{E} , we expand the dimension corresponding to \mathbf{x} and add a cluster prior. The objective matrix formula is derived as follows:

$$\mathbf{r} = \mathbf{I}_s \mathbf{x}_s + \boldsymbol{\varepsilon} \quad (23)$$

where $\mathbf{I}_s \in \mathbb{C}^{N \times 4(P-1)(Q-1)}$ denotes the new mapping matrix expanded from the identity matrix $\mathbf{E} \in \mathbb{C}^{N \times N}$. The cluster prior addition and expansion of its second dimension are similar to \mathbf{x} .

The adjacent elements of \mathbf{x}_s have the same prior and clustering hyperparameter α_{si} , and the PDF is expressed as follows:

$$P(\mathbf{x}_s|\boldsymbol{\alpha}_s, \sigma^2) = \prod_{i=1}^{N-3} P(x_{si}|\alpha_{si}, \sigma^2) \prod_{i=1}^{N-3} P(x_{s,i+1}|\alpha_{si}, \sigma^2) \prod_{i=1}^{N-3} P(x_{s,i+2}|\alpha_{si}, \sigma^2) \prod_{i=1}^{N-3} P(x_{s,i+3}|\alpha_{si}, \sigma^2). \quad (24)$$

Referring to the solution of MT-BCS [30], [31], we integrate the posterior distribution $P(\mathbf{x}_s|\boldsymbol{\alpha}_s, \sigma^2)$ of hyperparameter σ^2 , and the mean value $\boldsymbol{\mu}_s$ and variance $\boldsymbol{\Sigma}_s$ are obtained as follows:

$$\mathbf{A} = \text{diag}(\boldsymbol{\alpha}_s) \quad \boldsymbol{\Sigma}_s = (\mathbf{A} + \mathbf{I}_s^T \mathbf{I}_s)^{-1} \quad \boldsymbol{\mu}_s = \boldsymbol{\Sigma}_s \mathbf{I}_s^T \mathbf{r}. \quad (25)$$

We then focus on the point estimation of $\boldsymbol{\alpha}$, which is determined by maximizing the logarithm likelihood. The fast algorithm of the maximum likelihood is decomposed as follows:

$$\begin{aligned} \mathcal{L}(\boldsymbol{\alpha}_s) &= -(a + N) \log (\mathbf{r}^H \mathbf{C}^{-1} \mathbf{r} + 2b) - \frac{1}{2} \log |a| + \text{const} \\ &= \mathcal{L}(\boldsymbol{\alpha}_{s,-i}) + \ell(\alpha_{si}) \end{aligned} \quad (26)$$

where $\mathbf{C} = \mathbf{I}_4 + \mathbf{I}_s \mathbf{A}^{-1} \mathbf{I}_s$ and \mathbf{I}_4 is a 4×4 all-ones matrix, and $\mathcal{L}(\boldsymbol{\alpha}_{s,-i})$ is the same as $\mathcal{L}(\boldsymbol{\alpha}_s)$, except the i th component $\ell(\alpha_{si})$ is removed. By expanding \mathbf{C}^{-1} with the inverse matrix lemma and substituting it into (26), the point estimation is obtained as follows:

$$\begin{aligned} \ell(\alpha_{si}) &= -(a + N) \log \left[1 - \frac{1}{g_i} \mathbf{q}_i^H (\mathbf{s}_i + \alpha_{si} \mathbf{I}_4)^{-1} \mathbf{q}_i \right] \\ &\quad - \log |\mathbf{I}_4 + \alpha_{si}^{-1} \mathbf{s}_i| \end{aligned} \quad (27)$$

with

$$\begin{aligned} g_i &= \mathbf{r}^H \mathbf{C}_{-i}^{-1} \mathbf{r} + 2d, \quad \mathbf{s}_i = \mathbf{I}_{si}^T \mathbf{C}_{-i}^{-1} \mathbf{I}_{si} \\ \mathbf{q}_i &= \mathbf{I}_{si}^T \mathbf{C}_{-i}^{-1} \mathbf{r}. \end{aligned} \quad (28)$$

As \mathbf{I}_{si} and $\mathbf{I}_{s,i+1\dots}$ are composed of adjacent elements of the identity matrix, they are similar to each other. Therefore, \mathbf{s}_i can be approximated as $s_i \mathbf{I}_4$. Point estimate $\ell(\alpha_{si})$ is approximated as follows:

$$\tilde{\ell}(\alpha_{si}) = -(a + N) \log \left(1 - \frac{\|\mathbf{q}_i\|^2/g_i}{\alpha_{si} + 4s_i} \right) - \log (4\alpha_{si}^{-1}s_i + 1). \quad (29)$$

When $\tilde{\ell}(\alpha_{si})$ reaches the maximum value, α_{si} is the optimal solution. We differentiate $\tilde{\ell}(\alpha_{si})$ and set it to zero to derive the

solution of α_{si} as follows:

$$\alpha_{si} = \begin{cases} \frac{4s_i(4s_i - \|q_i\|^2/g_i)}{(a+N)\|q_i\|^2/g_i - 4s_i}, & \frac{4s_i(4s_i - \|q_i\|^2/g_i)}{(a+N)\|q_i\|^2/g_i - 4s_i} > 0 \\ +\infty, & \text{otherwise.} \end{cases} \quad (30)$$

Considering that α_{si} is nonnegative, we set it to $+\infty$ when it is negative. This causes the posterior of x_s to be centered at zero, thus excluding an unsuitable target. α_s can be solved efficiently using the fast relevance vector machine (RVM) method. The element of α is contained in four elements in α_s , and α_i is derived from α_s as follows:

$$\alpha_i = \begin{cases} +\infty, & \min(\alpha_{si}, \alpha_{s,i-1}, \alpha_{s,i-2}, \alpha_{s,i-3}) = +\infty \\ 1/(\frac{1}{\alpha_{si}} + \frac{1}{\alpha_{s,i+1}} + \frac{1}{\alpha_{s,i+2}} + \frac{1}{\alpha_{s,i+3}}), & \text{otherwise} \end{cases} \quad (31)$$

C. Nesterov's Accelerated Update

Once the aforementioned probability mapping module outputs $x^{(k)}$, the initial value of the next iteration is updated using Nesterov's acceleration method, which is a momentum update method. The formula for Nesterov's accelerated update is given by

$$t^{(k+1)} = \frac{1}{2} \left(1 + \sqrt{1 + 4t^{(k)}^2} \right) \quad (32)$$

$$y^{(k+1)} = x^{(k)} + \frac{t^{(k)} - 1}{t^{(k+1)}} (x^{(k)} - x^{(k-1)}) \quad (33)$$

where $t^{(k)}$ indicates the momentum update scale and $y^{(k+1)}$ indicates the initial value of the next iteration. This method essentially uses the second-order gradient of the objective function and can effectively accelerate the convergence [26], [32].

IV. EXPERIMENTAL RESULTS

In this section, the results of several experiments are given to verify the performance of the proposed CFISTA in complex-valued deconvolution beamforming. All experiments were conducted using MATLAB R2021b with an Intel i5-12600K CPU and 32 GB of RAM.

A. Beam Resolution Performance of Coherent Targets

In this simulation, we compared the performance of DAMAS2, FFT-NNLS, RL, CLEAN, FISTA, and CFISTA for planar arrays to demonstrate the superiority of CFISTA in terms of beam resolution. The planar array imaging sonar parameters are listed in Table I.

We conducted an experiment on the block-clustering targets. There were six clusters of targets, each with two adjacent targets separated by 1.5° . The center beam of the observation domain was considered the origin; thus, the six clusters of targets were symmetrical to $(\pm 10^\circ, 0^\circ)$, $(-10^\circ, \pm 10^\circ)$, and $(10^\circ, \pm 10^\circ)$. We set the elements that correspond to the target directions in x to 1 as the ground truth. The targets were located in far-field.

CBF results are shown in Fig. 4, and the beams were normalized with the ideal target intensity of 0 dB. The beams pointed toward each target; however, the two beams from adjacent targets could not be distinguished, and many high-intensity sidelobes existed.

TABLE I
PLANAR ARRAY IMAGING SONAR PARAMETERS

Transmitted Signal Frequency	300 kHz
Transmitted Pulse	Continuous Wave
Transmitted Signal Wavelength	$\lambda = 5$ mm
Receiving Element Number	$M = 2304$, $R = 48$, $C = 48$
Receiving Element Spacing	$d_x = 2.5$ mm, $d_y = 2.5$ mm
Desired Directions	$N = 129 \times 129$
Scan Range	$60^\circ \times 60^\circ$

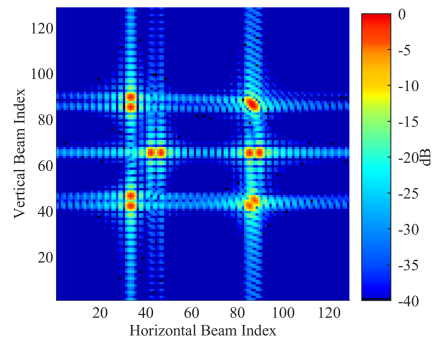


Fig. 4. CBF normalized beam pattern with six clusters of targets (each cluster has two adjacent targets).

The performances of the proposed and conventional deconvolution methods are depicted in Fig. 5. The iteration number of CFISTA was set to five. For the conventional methods, the number of iterations was set to 1000 to ensure that the results converged.

As shown in Fig. 5, all methods are considerably better than CBF. However, except for CFISTA, there were beam power leakages around each target and superposition to sidelobes. In the conventional methods, the two beams around $(10^\circ, 10^\circ)$ were not correctly distinguished and were merged into a stronger single beam. Among these, only CFISTA fully distinguished all the adjacent beams. Notably, FISTA had the best imaging quality among the conventional methods because of the fewer scattered sidelobes; however, high-intensity sidelobes existed around the main lobes. Conversely, the proposed CFISTA inherited the advantages of FISTA and completely suppressed the strong sidelobes because of its better matching model. Due to the utilization of complex-valued information and the optimized gradient descent and probability mapping, CFISTA achieves superior performance to compared methods with fewer iterations.

To visually compare the deconvolution results, we extracted the vertical beams at -10° , as shown in Fig. 6. The results show that the beam intensity of the intensity-based deconvolution methods is lower than that of the targets and CBF. It is caused by the nonnegative beam intensity constraint of these methods. This implies that when CBF beam intensity is lower than the value of the targets, the intensity-based methods are limited and cannot accurately estimate the targets. Conversely, CFISTA operates in a complex domain and is not restricted by the constraint.

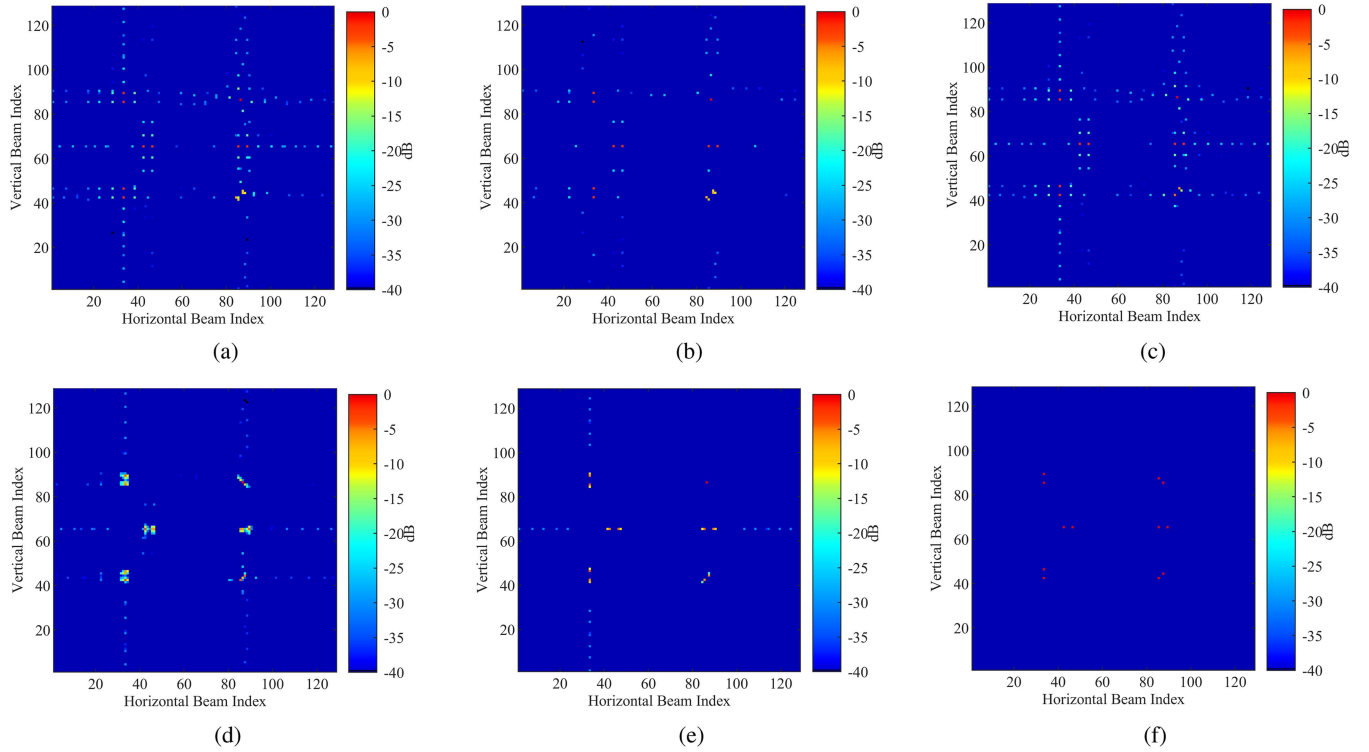


Fig. 5. Top view of the normalized deconvolution beam pattern of the proposed and conventional methods with six target clusters. (a) DAMAS2. (b) FFT-NNLS. (c) CLEAN. (d) RL. (e) FISTA. (f) CFISTA.

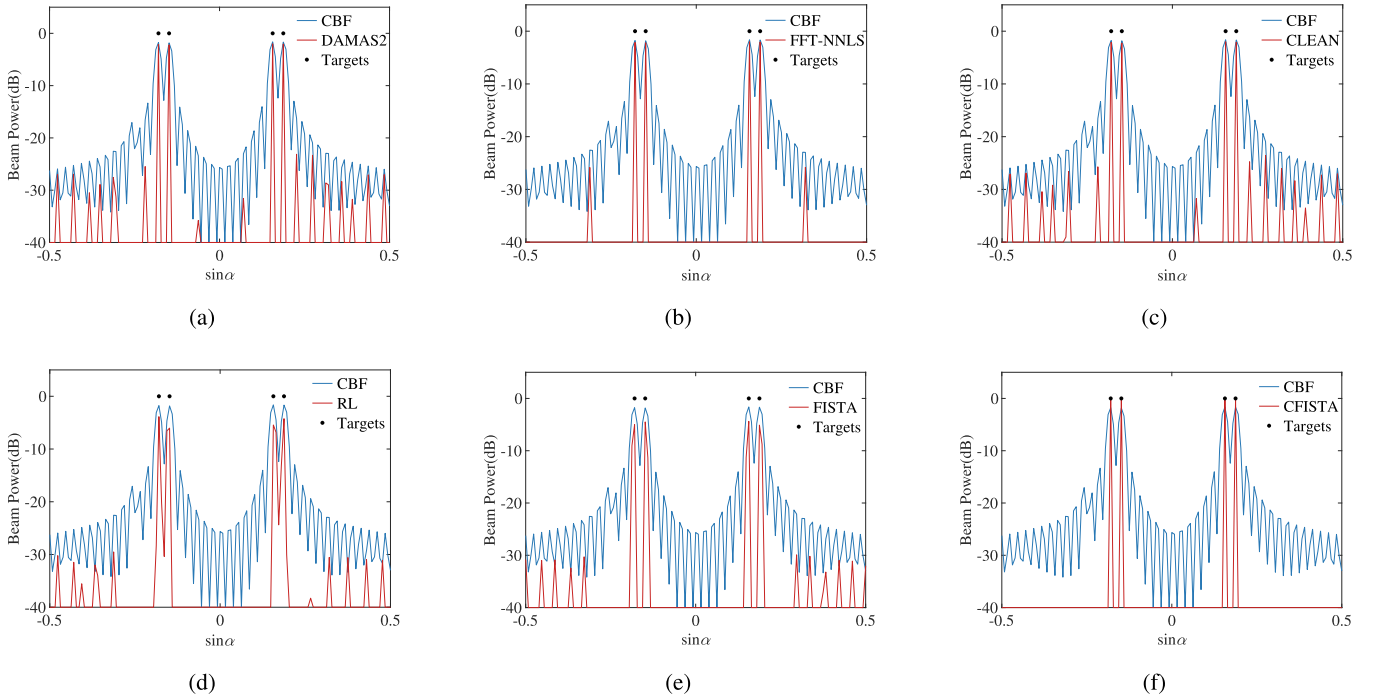


Fig. 6. Slice of 65th horizontal beams. (a) DAMAS2. (b) FFT-NNLS. (c) CLEAN. (d) RL. (e) FISTA. (f) CFISTA.

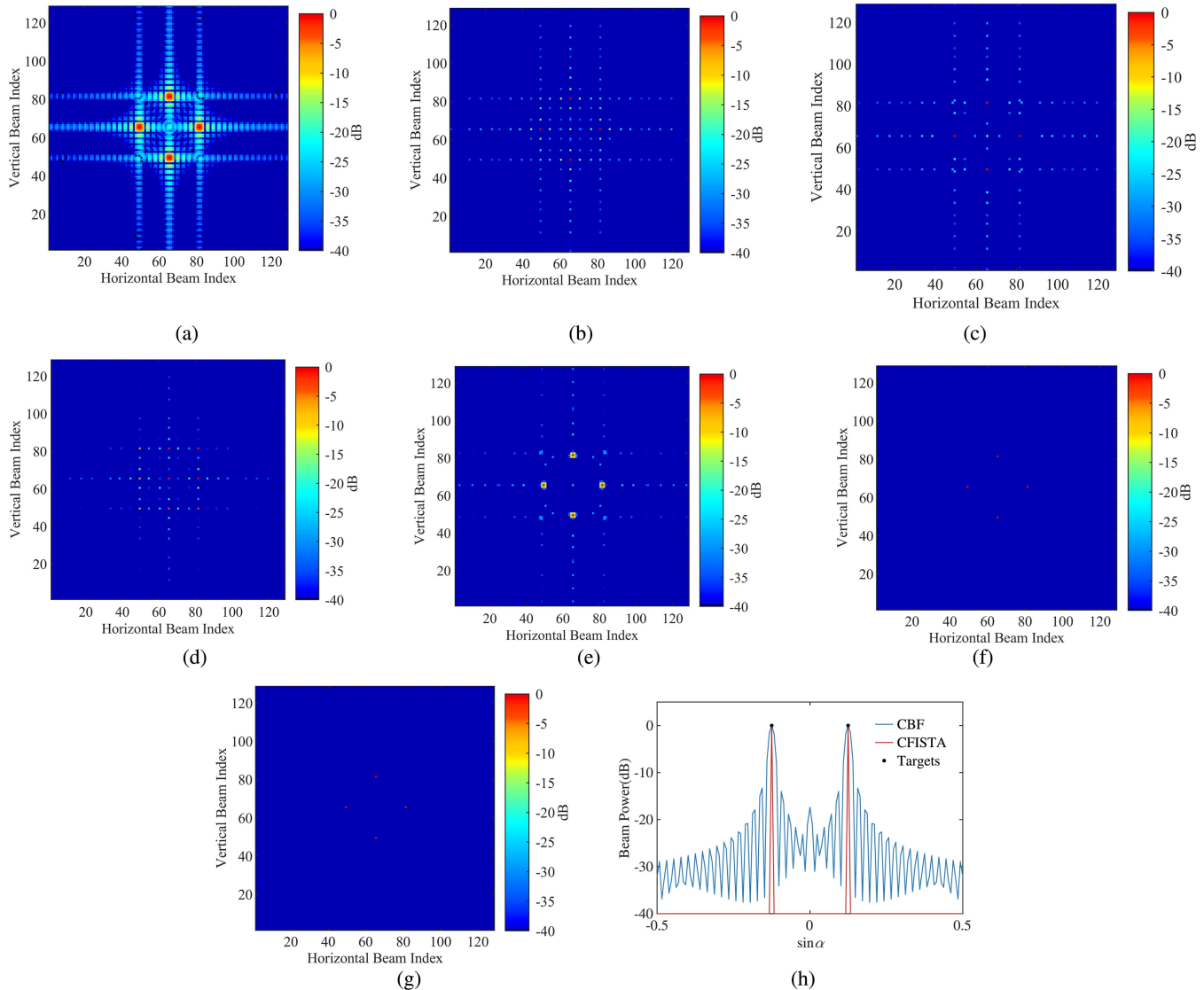


Fig. 7. Beam patterns of nonclustered targets without adding noise. (a) CBF. (b) DAMAS2. (c) FFT-NNLS. (d) CLEAN. (e) RL. (f) FISTA. (g) CFISTA. (h) Slice of the 65th horizontal beams.

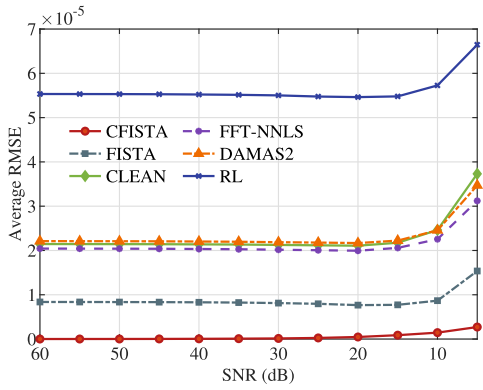


Fig. 8. Normalized average root mean square error (RMSE) results for SNR values of 5–60 dB.

The probability model directly estimates the distribution and intensity of the targets, and the beam results are closer to the ideal value.

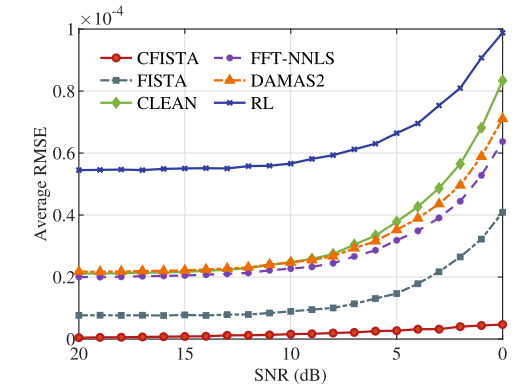


Fig. 9. Normalized average RMSE results for SNR values from 0 to 20 dB.

The average 3-dB main lobe width, sidelobe suppression ratio, and normalized RMSE using a synthetic target distribution are listed in Table II to analyze the performance of CFISTA.

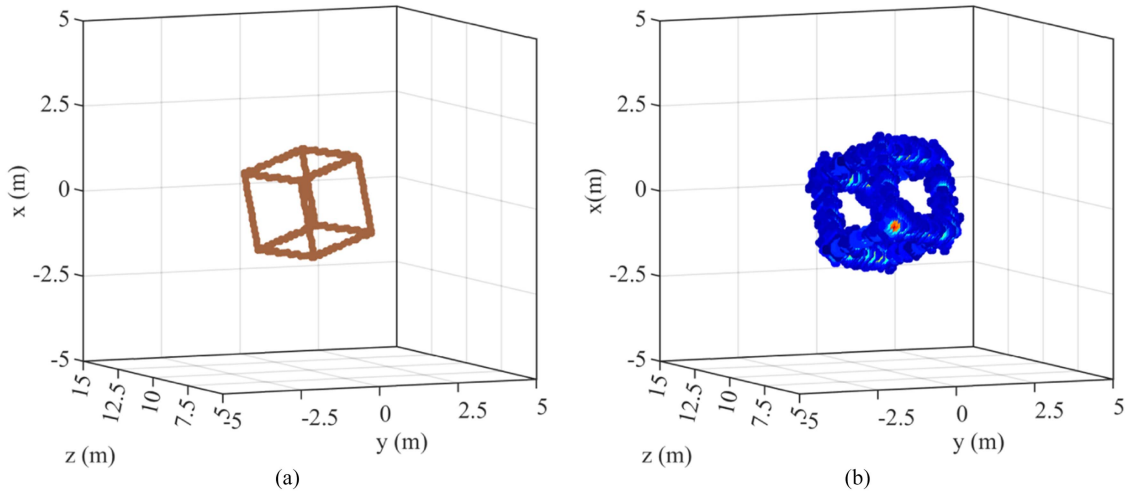


Fig. 10. 3-D deconvolution beamforming target and CBF result. (a) Synthetic target (cube frame). (b) CBF result.

TABLE II
MAIN METRICS FOR BEAM PERFORMANCE

Method	3-dB main lobe width	Sidelobe Suppression Ratio	Normalized RMSE
CBF	0.965°	1.807 dB	0.0258
DAMAS2	0.133°	9.924 dB	2.931×10^{-4}
FFT-NNLS	0.125°	9.942 dB	3.551×10^{-5}
CLEAN	0.095°	16.037 dB	2.348×10^{-4}
RL	0.315°	6.826 dB	4.606×10^{-4}
FISTA	0.287°	8.785 dB	1.078×10^{-4}
CFISTA	0.065°	≥ 40 dB	9.218×10^{-6}

Based on the results, CFISTA reduced the main lobe beamwidth and improved the sidelobe suppression ratio. Owing to the complete elimination of the sidelobes and almost no power loss in the main lobe, the RMSE of CFISTA is one or two orders of magnitude lower than that of other methods. Compared with conventional deconvolution beamforming methods, CFISTA has notable advantages in terms of the main lobe width and sidelobe suppression, proving that its beam resolution is higher.

B. Noise Robustness

To further verify the noise immunity of the proposed CFISTA, a noise term was added to the CBF results. We set four separate points as the targets, and the random noise term follows a zero-mean Gaussian distribution.

The spacing between targets was increased to reduce the energy overlap of the beam between closely spaced targets, thereby avoiding the distortion of the main lobe that could potentially affect intensity-based methods [33]. The four targets were located at $(0^\circ, \pm 7.5^\circ)$ and $(\pm 7.5^\circ, 0^\circ)$ in far-field, and the

intensity was set to 1. The beam pattern of nonclustered targets without adding noise is shown in Fig. 7.

When the targets are nonclustered, all deconvolution methods, except CLEAN, can clearly distinguish the target beams. However, problems such as insufficient sidelobe suppression, and wide main lobes remain. The performance of FISTA is the best among intensity-based methods, and its RMSE is 1.28×10^{-8} . As for CFISTA, its RMSE is 7.46×10^{-11} , indicating that the CFISTA result is consistent with the ideal target distribution. A comparison of beam patterns and the beam slice proves that CFISTA outperforms intensity-based deconvolution beamforming methods.

Subsequently, the average normalized RMSE of the synthetic beams and deconvolution results with different signal-to-noise ratios (SNRs) were compared. The noise variance was gradually increased, and the SNR was reduced from 60 to 5 dB in 5-dB intervals. In addition, 100 random experiments were performed for each SNR value to eliminate the influence of the random seeds. The results of the average normalized RMSE for different SNR values are shown in Fig. 8.

When the beam intensity is much higher than the noise (i.e., SNR is more than 20 dB), the RMSE values of all methods were basically unchanged. As previously mentioned, CFISTA has excellent sidelobe suppression ability; therefore, it can effectively eliminate the interference of noise in the beam pattern after deconvolution. The RMSE of CFISTA is approximately 5% that of the other methods. Once the noise is increased (i.e., SNR is less than 20 dB), conventional intensity-based methods become ineffective in suppressing irregular sidelobes generated by strong noise; thus, the RMSE increases significantly with the noise.

A simulation of the RMSE with a low SNR was performed to verify the robustness of the proposed method in an environment with strong background noise. The results of the average normalized RMSE with SNR values from 0 to 20 dB are shown in Fig. 9.

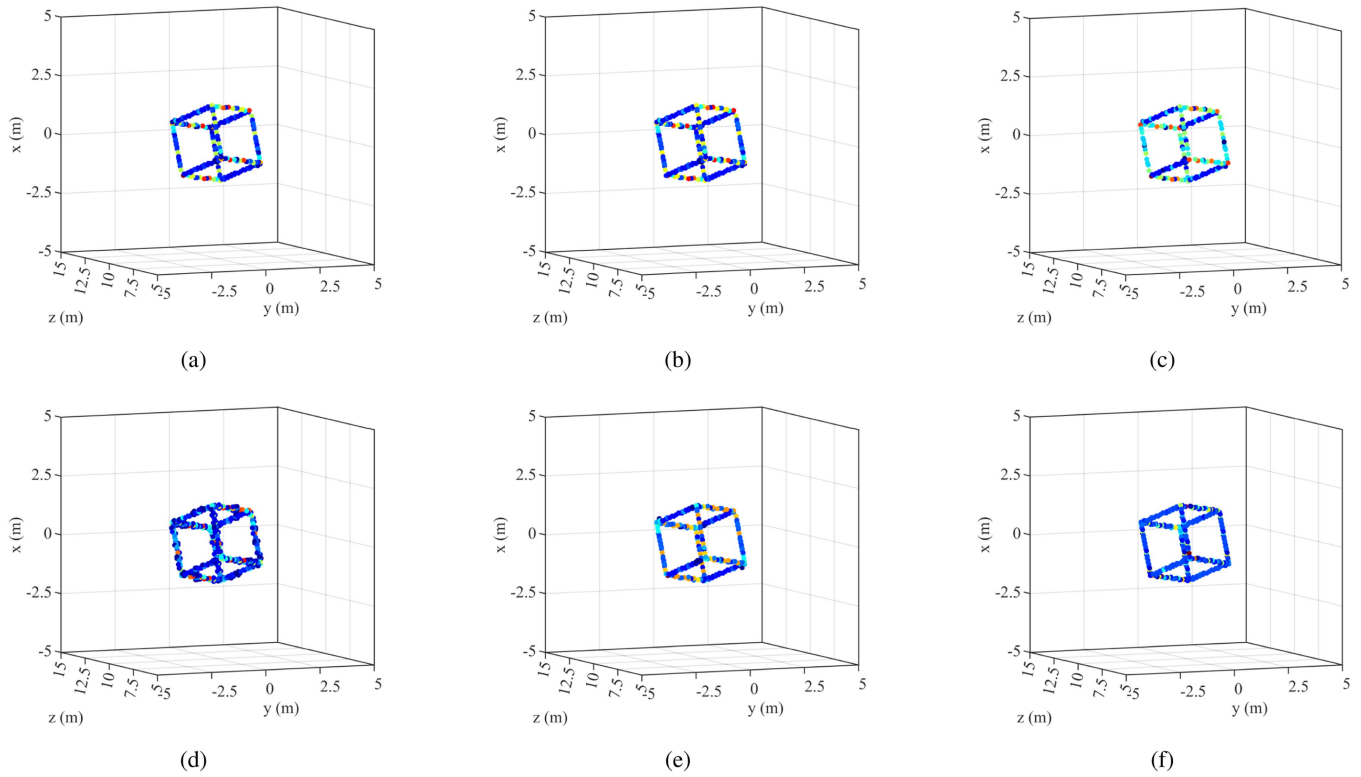


Fig. 11. 3-D cube frame target simulation results. (a) FFT-NNLS. (b) DAMAS2. (c) CLEAN. (d) RL. (e) FISTA. (f) CFISTA.

FFT-NNLS, DAMAS2, and FISTA were based on linear inverse problems, and the trends of their RMSE–SNR curves were similar. Among them, FISTA had a lower RMSE because it could better eliminate the cluttered beams. CLEAN reconstructed the strongest beam in each iteration, and the deconvolution beamforming effect was poor when noise was enhanced. RL is a probabilistic-based approach that is less stable when models are mismatched; thus, its RMSE increases the fastest.

Among all methods, the proposed CFISTA for deconvolution beamforming achieved the best robustness in noise, in which the average RMSE with an SNR value of 0 dB was approximately 10% of that of the conventional method with the smallest RMSE.

C. Simulation of Cube Frame as the Target

For 3-D sonars, a 3-D underwater image is composed of a series of 2-D beam patterns in the direction of observation. The previous simulations were classified as monolayer 2-D deconvolution beamforming. In this section, the results of a 3-D target simulation are presented and analyzed to further investigate the deconvolution beamforming performance of the deconvolution methods.

The synthetic target was a cube frame with a side length of 2.4 m and rotation of 30° along the horizontal and vertical axes. It was composed of randomly scattered points with spacing smaller than $1/4\lambda$ and uniform intensity [34]. The parameters of the planar array imaging sonar are listed in Table I. The target was located 10 m from the array, indicating that it was in the far field of the array. At this distance, the edge of the target accounts for about 30-beam intervals. And the spacing between

each 2-D beam plane was 0.08 m. The target and CBF results in the Cartesian coordinate are shown in Fig. 10. Neglecting distance loss, the ideal beam intensity of the target is expected to be consistent. The CBF results were normalized, as shown in Fig. 10(b), in which each edge contains more data points and becomes thicker than the synthetic target.

Fig. 11 shows the results of the cube frame processed by the deconvolution beamforming methods. The colors in Figs. 10(b) and 11 of CBF and deconvolution methods represent the different intensity values of the normalized beam points in jet colormap. The numbers of deconvolution beamforming iterations per layer of the conventional methods and CFISTA were the same as before. As shown in Fig. 11(f), the CFISTA exhibits better consistency in the intensity values of the beam points, which are closer to the ideal targets depicted in Fig. 10(a).

The peak SNR (PSNR) was used to quantitatively measure the image quality after deconvolution beamforming. The running time was also compared. The PSNR and running times are listed in Table III.

As evident from Table III, despite the slightly increased computational load per iteration resulting from more accurate mapping and complex gradients, CFISTA still maintains an advantage in overall runtime compared to methods other than CLEAN, and it exhibits the highest PSNR among all the methods. The running time of CLEAN is much faster than that of other methods because its principle is to recover the maximum beam one by one without matrix multiplication. For the methods based on linear inverse problems, the running time of CFISTA is slightly longer than that of DAMAS2, and the PSNR of CFISTA is about 2.5–4 dB higher than that of the compared methods.

TABLE III
PSNR AND RUNNING TIME OF THE DIFFERENT METHODS IN THE
3-D TARGET SIMULATION

Method	PSNR (dB)	Running Time (s)
DAMAS2	44.2452	33.635
FFT-NNLS	45.0744	99.473
CLEAN	43.7297	0.906
RL	43.2306	67.006
FISTA	45.1383	66.524
CFISTA	47.6228	34.166

V. CONCLUSION

This study proposed a complex-valued FSITA method to improve the beam resolution in deconvolution beamforming. Complex gradient descent and multiple-task probability mapping were applied to the FISTA to extend the method to the complex domain. Cluster prior and FFT methods were combined to accurately and efficiently model coherent narrowband sonar signals.

The simulation results for the planar array revealed that CFISTA has a superior main lobe width, sidelobe suppression, and RMSE with ground truth compared to those of the conventional deconvolution methods. Moreover, CFISTA showed significantly higher noise immunity in multiple SNR scenarios, better beamforming quality, and shorter running time in the 3-D target simulation than those of the other methods.

In the future, the adaptive scale of cluster prior and learnable momentum update parameters will be studied to further improve the accuracy of deconvolution.

REFERENCES

- [1] D. H. Johnson and D. E. Dudgeon, "Beamforming," in *Array Signal Processing: Concepts and Techniques*. Englewood Cliffs, NJ, USA: Prentice-Hall, 1993, ch. 4.
- [2] A. Macovski, "Ultrasonic imaging using arrays," *Proc. IEEE*, vol. 67, no. 4, pp. 484–495, 1979.
- [3] H. L. Van Trees, "Planar arrays and apertures," in *Optimum Array Processing: Part IV of Detection, Estimation, and Modulation Theory*. Hoboken, NJ, USA: Wiley, 2002, ch. 4.
- [4] M. Palmese and A. Trucco, "Three-dimensional acoustic imaging by chirp zeta transform digital beamforming," *IEEE Trans. Instrum. Meas.*, vol. 58, no. 7, pp. 2080–2086, Jul. 2009.
- [5] D. Zhao, X. Liu, W. Chen, and Y. Chen, "Optimized design for sparse cross arrays in both near-field and far-field," *IEEE J. Ocean. Eng.*, vol. 44, no. 3, pp. 783–795, Jul. 2019.
- [6] Z. Lin, Y. Chen, X. Liu, R. Jiang, and B. Shen, "A Bayesian compressive sensing-based planar array diagnosis approach from near-field measurements," *IEEE Antennas Wireless Propag. Lett.*, vol. 20, no. 2, pp. 249–253, Feb. 2021.
- [7] O. Lylloff, E. Fernández-Grande, F. Agerkvist, J. Hald, E. T. Roig, and M. S. Andersen, "Improving the efficiency of deconvolution algorithms for sound source localization," *J. Acoustical Soc. Amer.*, vol. 138, no. 1, pp. 172–180, 2015.
- [8] P. Wang, C. Chi, P. Zhang, L. Wei, J. Liu, and H. Huang, "High-resolution underwater 3D acoustical imaging via deconvolved conventional beamforming," in *Proc. IEEE Glob. Oceans*, 2020, pp. 1–4.
- [9] M. Slawski and M. Hein, "Non-negative least squares for high-dimensional linear models: Consistency and sparse recovery without regularization," *Electron. J. Statist.*, vol. 7, pp. 3004–3056, 2013.
- [10] R. Dougherty, "Extensions of DAMAS and benefits and limitations of deconvolution in beamforming," in *Proc. 11th AIAA/CEAS Aeroacoustics Conf.*, 2005, Paper 2961.
- [11] T. F. Bergh, "Deconvolution approach to the mapping of acoustic sources with matching pursuit and matrix factorization," *J. Sound Vib.*, vol. 459, 2019, Art. no. 114842.
- [12] M. Wei and L. Xun, "Improving the efficiency of DAMAS for sound source localization via wavelet compression computational grid," *J. Sound Vib.*, vol. 395, pp. 341–353, 2017.
- [13] T. F. Brooks and W. M. Humphreys, "A deconvolution approach for the mapping of acoustic sources (DAMAS) determined from phased microphone arrays," *J. Sound Vib.*, vol. 294, no. 4/5, pp. 856–879, 2006.
- [14] K. Ehrenfried and L. Koop, "Comparison of iterative deconvolution algorithms for the mapping of acoustic sources," *AIAA J.*, vol. 45, no. 7, pp. 1584–1595, 2007.
- [15] T. Yang, "Deconvolved conventional beamforming for a horizontal line array," *IEEE J. Ocean. Eng.*, vol. 43, no. 1, pp. 160–172, Jan. 2018.
- [16] T. Zhou, J. Huang, W. Du, J. Shen, and W. Yuan, "2-D deconvolved conventional beamforming for a planar array," *Circuits, Syst., Signal Process.*, vol. 40, no. 11, pp. 5572–5593, 2021.
- [17] J. Tsao and B. D. Steinberg, "Reduction of sidelobe and speckle artifacts in microwave imaging: The CLEAN technique," *IEEE Trans. Antennas Propag.*, vol. 36, no. 4, pp. 543–556, Apr. 1988.
- [18] P. Sijtsma, "Clean based on spatial source coherence," *Int. J. Aeroacoustics*, vol. 6, no. 4, pp. 357–374, 2007.
- [19] T. J. Cornwell, "Multiscale CLEAN deconvolution of radio synthesis images," *IEEE J. Sel. Topics Signal Process.*, vol. 2, no. 5, pp. 793–801, Oct. 2008.
- [20] R. Bose, "Lean CLEAN: Deconvolution algorithm for radar imaging of contiguous targets," *IEEE Trans. Aerosp. Electron. Syst.*, vol. 47, no. 3, pp. 2190–2199, Jul. 2011.
- [21] L. Zhang, L. Xu, and M. Zhang, "Parameterized clean deconvolution in radio synthesis imaging," *Pub. Astronomical Soc. Pacific*, vol. 132, no. 1010, 2020, Art. no. 041001.
- [22] A. Beck and M. Teboulle, "A fast iterative shrinkage-thresholding algorithm for linear inverse problems," *SIAM J. Imag. Sci.*, vol. 2, no. 1, pp. 183–202, 2009.
- [23] S. Valaee, B. Champagne, and P. Kabal, "Parametric localization of distributed sources," *IEEE Trans. Signal Process.*, vol. 43, no. 9, pp. 2144–2153, Sep. 1995.
- [24] V. Murino and A. Trucco, "Three-dimensional image generation and processing in underwater acoustic vision," *Proc. IEEE*, vol. 88, no. 12, pp. 1903–1948, Dec. 2000.
- [25] A. Xenaki, F. Jacobsen, and E. Fernandez-Grande, "Improving the resolution of three-dimensional acoustic imaging with planar phased arrays," *J. Sound Vib.*, vol. 331, no. 8, pp. 1939–1950, 2012.
- [26] Y. E. Nesterov, "A method of solving a convex programming problem with convergence rate $O(k^2)$," in *Doklady Akademii Nauk*, vol. 269, no. 3, pp. 543–547, 1983.
- [27] R. Gribonval, "Should penalized least squares regression be interpreted as maximum a posteriori estimation?," *IEEE Trans. Signal Process.*, vol. 59, no. 5, pp. 2405–2410, May 2011.
- [28] D. Ito, S. Takabe, and T. Wadayama, "Trainable ISTA for sparse signal recovery," *IEEE Trans. Signal Process.*, vol. 67, no. 12, pp. 3113–3125, Jun. 2019.
- [29] S. Takabe, T. Wadayama, and Y. C. Eldar, "Complex trainable ISTA for linear and nonlinear inverse problems," in *Proc. IEEE Int. Conf. Acoust., Speech, Signal Process.*, 2020, pp. 5020–5024.
- [30] M. E. Tipping, "Sparse Bayesian learning and the relevance vector machine," *J. Mach. Learn. Res.*, vol. 1, pp. 211–244, 2001.
- [31] S. Ji, D. Dunson, and L. Carin, "Multitask compressive sensing," *IEEE Trans. Signal Process.*, vol. 57, no. 1, pp. 92–106, Jan. 2009.
- [32] B. Shi, S. S. Du, M. I. Jordan, and W. J. Su, "Understanding the acceleration phenomenon via high-resolution differential equations," *Math. Program.*, pp. 1–70, 2021.
- [33] Q. Leclerc, A. Pereira, C. Bailly, J. Antoni, and C. Picard, "A unified formalism for acoustic imaging based on microphone array measurements," *Int. J. Aeroacoustics*, vol. 16, no. 4/5, pp. 431–456, 2017.
- [34] M. Palmese and A. Trucco, "Acoustic imaging of underwater embedded objects: Signal simulation for three-dimensional sonar instrumentation," *IEEE Trans. Instrum. Meas.*, vol. 55, no. 4, pp. 1339–1347, Aug. 2006.



Shiyao Jiang was born in Zhejiang, China, in 1997. He received the B.Sc. degree in electrical engineering from Zhejiang University, Hangzhou, China, in 2019, where he is currently working toward the Ph.D. degree in electronic information technology and instrument.

His major research interests include array signal processing, beamforming algorithm, and embedded system design.



Boxuan Gu was born in Hubei, China, in 1992. He received the B.Sc. and Ph.D. degrees in engineering instrument science and technology from Zhejiang University, Hangzhou, China, in 2014 and 2021, respectively.

He is currently a Postdoctor with Zhejiang University. His major research interests include sonar signal processing, parallel processing, and embedded system design.



Rongxin Jiang was born in Hunan, China, in 1982. He received the B.Sc. and Ph.D. degrees in computer vision from Zhejiang University, Hangzhou, China, in 2002 and 2008, respectively.

He is currently an Associate Professor with Zhejiang University. His major research interests include computer vision and networking.



Yaowu Chen was born in Heilongjiang, China, in 1963. He received the Ph.D. degree in embedded system from Zhejiang University, Hangzhou, China, in 1998.

He is currently a Professor and the Director of the Institute of Advanced Digital Technologies and Instrumentation, Zhejiang University. His major research interests include embedded system, multimedia system, and networking.



Xuesong Liu was born in Shaanxi, China, in 1988. He received the B.Sc. and Ph.D. degrees in sonar signal processing from Zhejiang University, Hangzhou, China, in 2010 and 2015, respectively.

He is currently an Associate Professor with Zhejiang University. His current research interests include sonar signal processing, parallel processing, and embedded system design.